文章编号：1001-9014(2024)05-0603-06

DOI:10.11972/j.issn.1001-9014.2024.05.003

Long wavelength infrared metalens fabricated by photolithography

LI Yun-Peng[1,2,4], LUO Jia-Cheng[2,3,4], JI Ruo-Nan[2,4], XIE Mao-Bin[2,4,5], CUI Wen-Nan[2], WANG Shao-Wei[2,4,5*], LIU Feng[3*], LU Wei[1,2,4,5]

(1. School of Physical Science and Technology, ShanghaiTech University, Shanghai 201210, China;
2. State Key Laboratory of Infrared Physics, Shanghai Institute of Technical Physics, Chinese Academy of Sciences, Shanghai 200083, China;
3. Department of Physics, Shanghai Normal University, Shanghai 200234, China;
4. Shanghai Engineering Research Center of Energy-Saving Coatings, Shanghai 200083, China;
5. University of Chinese Academy of Sciences, Beijing 100049, China)

Abstract: Metasurfaces in the long wave infrared (LWIR) spectrum hold great potential for applications in thermal imaging, atmospheric remote sensing, and target identification, among others. In this study, we designed and experimentally demonstrated a 4 mm size, all-silicon metasurface metalens with large depth of focus operational across a broadband range from 9 μm to 11.5 μm. The experimental results confirm effective focusing and imaging capabilities of the metalens in LWIR region, thus paving the way for practical LWIR applications of metalens technology.

Key words: long wave infrared, broadband operation, passive imaging

光刻法制备的长波红外超透镜

李云鹏[1,2,4], 罗嘉诚[2,3,4], 冀若楠[2,4], 谢茂彬[2,4,5], 崔文楠[2], 王少伟[2,4,5*], 刘 锋[3*], 陆 卫[1,2,4,5]

(1. 上海科技大学物质科学与技术学院, 上海 201210;
2. 中国科学院上海技术物理研究所 红外物理国家重点实验室, 上海 200083;
3. 上海师范大学物理系, 上海 200234;
4. 上海节能镀膜玻璃工程技术研究中心, 上海 200083;
5. 中国科学院大学, 北京 100049)

摘要:长波红外的超表面在热成像、大气遥感和目标识别等领域具有巨大的应用潜力。在这项研究中,我们设计并实验展示了一种 4 mm 尺寸的全硅超表面透镜,其具有大焦深,可在 9 μm 至 11.5 μm 范围内工作。实验结果证实了超透镜在长波红外区域的有效聚焦和成像能力,为超透镜技术在长波红外领域的实际应用铺平了道路。

关 键 词:长波红外;宽带工作;被动成像

中图分类号:O43 **文献标识码**:A

Introduction

Miniaturized and lightweight imaging systems are fast becoming integral to consumer electronics, industrial, medical, and automotive sectors[1]. The optical lens, being the primary component of such systems, plays a crucial role in focusing light[2]. The atmospheric window of 9-11.5 μm is particularly significant due to the peak

Received date: 2024-03-11, **revised date**: 2024-06-19 **收稿日期**:2024-03-11,**修回日期**:2024-06-19

Foundation items: Supported by National Key R&D Program of China (2021YFA0715500), National Natural Science Foundation of China (NSFC) (12227901), Strategic Priority Research Program (B) of the Chinese Academy of Sciences (XDB0580000) and Chinese Academy of Sciences President's International Fellowship Initiative (2021PT0007).

Biography: LI Yun-Peng (1998-), Wei Fang, Master of Natural Science, Research area involves micro-nano photonics devices. Email: liyp1998@163.com.

* **Corresponding author**: wangshw@mail.sitp.ac.cn

of infrared radiation from room temperature object occurring at 10 μm, making this wavelength range vital for infrared imaging and detection[3]. However, traditional infrared lenses tend to be bulky, intricate, and thus counterproductive to the portability and accessibility of long-wave infrared (LWIR) devices. To correct chromatic aberration, these lenses need multiple lens groups, which inherently limits both the depth of focus(DOF) and imaging resolution. It also impedes its broadband performance and actual imaging ability[4].

Metasurfaces, artificially arranged nanostructures with sub-wavelength patterned layers[5, 6], have birthed a powerful new platform for light manipulation - the metalens. These metasurfaces control light characteristics such as amplitude, polarization, and phase[7-9], enabling metalenses to potentially resolve these issues and thereby streamline numerous infrared applications. This results in thinner[10], easier-to-align and package lenses[11], which in turn fosters a broad range of high-volume applications[12]. Metalenses have been widely reported for use in polarization regulation[13], beam shaping[14], holographic imaging[15], molecular fingerprint detection[16], integrated quantum devices[17] and more[18]. Yet, the majority of these studies focus on the visible[7, 19-25] and near-infrared[26-29] ranges, with mid-infrared and far-infrared metalenses still in their nascent stages of development[2, 30, 31].

Contrary to the short-wave range, LWIR requires higher imaging tolerances due to its all-weather applicability in military and security sectors, necessitating a larger DOF[32-36]. However, no reported metalenses can function wideband in the LWIR spectrum with an large DOF, due to inherent large dispersion, requiring specific wavelength light sources for active imaging[37, 38]. Lenses with larger DOF are more practical for real-world applications[32, 33] and can gather more object information and exhibit superior performance in broadband application scenarios, while increasing the DOF of a metalens typically sacrifices resolution[39, 40]. The reported methodologies that ostensibly realize expanded depth of focus include Fresnel lens arrays (FLAs), axial lenses (AXLs) and light sword optical elements (LSOEs)[41, 42].

Given the diverse and com plex requirements of long-wave infrared metalenses, including collecting more light for imaging, expanding the size of the metalens becomes essential[3]. However, most currently reported metalenses are relatively small and have short focal lengths[29] due to the complex design[6] and manufacturing precision required for larger sizes and longer focal lengths. These limitations necessitate the use of high-cost electron beam lithography for fabrication[1,43]. Further research has not been conducted on the potential wideband capabilities of existing LWIR metalenses[44]. The reported designs of large-scale metalenses have not considered their imaging tolerance[4, 45]. Our research addresses these challenges and contributes to the development of long-wave infrared metalenses with large DOF and broad band operation.

In the present study, we introduce a metalens with extensive DOF for LWIR focusing. Such a metalens is designed based on propagation phase modulation with silicon and can be realized through a straightforward single-step UV lithography process, which is capable of performing in the 9- 11. 5 μm wavelength range.

1 Design

The design of the unit cell must balance the high refractive index and low absorption of the material in use. Many of the cells employed in recent work are complex media, reducing their process compatibility. Our solution to these challenges is a silicon cylinder structure relying on propagation phase modulation. As illustrated in Fig. 1(a), the metalens is composed of circular silicon nanopillars arranged in a square lattice. The cell period P and cylinder height h are 6 μm, with cylinder radius R ranges from 1 μm to 2. 5 μm.

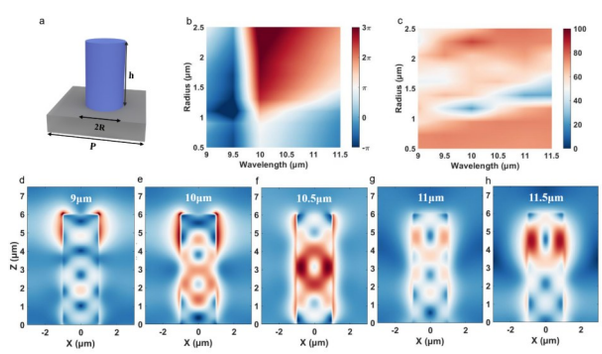

Fig. 1 The meta-atoms of metalens: (a) schematic diagram of designed meta-atoms; (b) the relationship between propagation phase and radius of meta-atoms in LWIR; (c) the transmission spectrum of meta-atoms in LWIR; (d) the electric field distribution of meta-atoms at wavelength of 9-11. 5 μm

图1 超透镜的超表面单元:(a)设计的超表面单元示意图;(b)长波红外中超表面单元的传输相位与半径的关系;(c)长波红外中超表面单元的透射谱;(d) 9~11. 5 μm波段内超表面单元的电场分布

Simulations performed using finite-difference time-domain (FDTD) methods demonstrate that the propagation phase can be adjusted by modifying the radius of the subwavelength meta-atoms. The propagation phase versus radius is displayed in Fig. 1(b). The silicon nanopillars showcase respectable transmission in the LWIR (9-11. 5μm) region, as evidenced in Fig. 1(c). The combination of low loss from the dielectric and an adept structural design allows for a superior overall transmittance at 10. 5 μm. Fig. 1(d) illustrates the electric field distribution $|E|$ of the silicon nanopillars with a diameter of 2 μm at wavelengths of 9-11. 5 μm. The strong optical energy confinement within the nanopillar implies that wavefront manipulation using meta-atoms is a localized effect. This capacity for wavefront regulation is achieved through the phase accumulation of the electric field within the silicon column, although it decreases when the operating wavelength is shifted, still maintains sufficient adjustment potential.

The ideal phase distribution $\varphi(x, y)$ of a metalens

can be expressed as Eq. (1)[46]:

$$\varphi(x,y,\lambda) = \frac{2\pi}{\lambda}\left(f - \sqrt{f^2 + x^2 + y^2}\right) \quad , \quad (1)$$

here, (x, y) denotes the spatial coordinates of the unit structure, λ represents the free space wavelength, and f is the focal length of the metalens. It can be understood from this equation that with the same radial distance and wavelength, a higher focal length results in a smaller geometric phase difference. This implies a higher requirement for phase regulation accuracy, substantially increasing the fabrication complexity.

For the metalens to have sufficient phase control capability and focusing efficiency, it's necessary that the metalens' meta-atoms can cover a phase of 2π, and that each meta-atom exhibits high transmittance. Based on the optical response results displayed in Fig. 1(b-c), we select the optimal structure as the phase cell library. We employ interpolation between transmittance phase and size to choose the meta-atoms, aiming to enhance the focusing performance[4]. Fig. S1 demonstrates the arrangement of our metalens units in a checkerboard layout, while Fig. S2 displays the phase distribution along the metalens radius.

The DOF of a lens can be generally expressed as per Eq. (2)[47]:

$$DOF = \frac{\lambda}{1 - \sqrt{1 - NA^2}} \quad , \quad (2)$$

where $NA = \sin[\arctan(D/(2f))]$, and D is incident aperture. To augment the DOF of the metalens, one can either reduce the incident aperture or increase the focal length. However, reducing the incident aperture will compromise the metalens resolution, while a significantly larger focal length will enlarge the entire optical system. Therefore, continuous optimization is required to select the appropriate incident aperture and focal length. According to Huygens' principle, the phase gradient over the surface of a metalens determines the propagation direction of the transmitted light[48]. We can manipulate the structural parameters of the meta-atom to subsequently alter its phase accumulation. By modifying the design of the metalens, it is feasible to induce more or less phase accumulation in some meta-atoms, facilitating the lengthwise broadening of focal spots. This configuration can be fabricated via a selective area etching effect.

We first designed a metalens structure with a central wavelength of 10.5 μm using the outlined method. Simulation results confirmed a commendable focusing effect and substantial DOF within the broadband range of 9-11.5 μm. Fig. 2(a-c) display the focusing impact of the metalens at wavelengths of 9 μm, 10 μm, and 10.5 μm. Correspondingly, the FWHM at these different wavelengths are 16.5, 16.3, 16.2 μm, respectively. The *NA* and focal length are 0.442, 0.445, 0.447 and 1.15 mm, 1.05 mm, 1 mm, respectively, corresponding to the DOF of 131, 126, 124 μm. Additionally, the metalens, due to its substantial DOF, enables a focus with minimal chromatic aberration at a specific position. This is due to the large overlapping area of the focal spot at varying wavelengths.

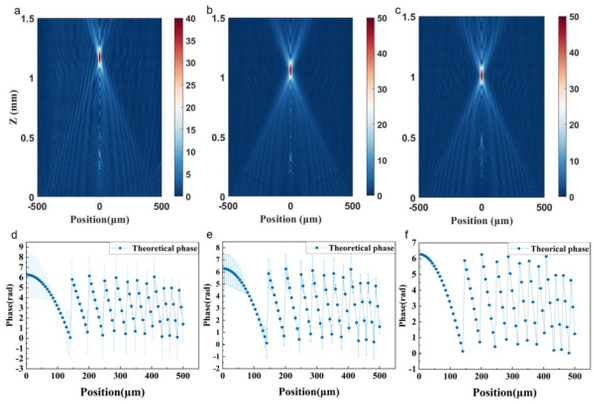

Fig. 2　The simulation results of metalens in 1 mm diameter: (a-c) simulated focusing effect at the operating wavelength of the 9, 10 and 10.5 μm for a metalens with a central wavelength of 10.5 μm; (d-f) comparison of the surface phase distribution of the metalens at 9, 10 and 10.5 μm. The dot plots are the theoretical surface phase distribution of the metalens with different operating wavelengths, and the error bar shows the deviation of the actual phase distribution

图 2　直径为 1 mm 的超透镜的模拟结果:(a-c)模拟的中心波长为 10.5 μm 的超透镜在 9、10 和 10.5 μm 工作波长下的聚焦效果;(d-f) 9、10 和 10.5 μm 处超透镜的表面相位分布比较。点阵图为不同工作波长下超透镜的理论表面相位分布,误差条为超透镜实际相位分布的偏差

Next, we studied the focusing deviation of the metalens during broadband operation. Fig. 2(d-f) compare the ideal phase distribution with the actual phase distribution of the designed metalens structure at wavelengths of 9 μm, 10 μm, and 10.5 μm. As the deviation between the actual operating wavelength and the theoretical design center wavelength increases from 0 to 1.5 μm, the propagation phase error of the meta-atoms also escalates. We computed the propagation phase error levels for all meta-atoms of the metalens operating at different wavelengths and quantified the percentage of each element with varying error sizes, as depicted in Fig. S3(in supplemental document). The maximum phase difference was observed to be 15%, signifying that the dispersion effect is minimal and broadband operation is feasible. We obtained similar results for 11 μm and 11.5 μm in Fig. S4(in supplemental document), also with minimal phase error levels.

2 Experiment

To enhance the practical application performance of the metalens, we designed a 4 mm diameter metalens with focal length of 4 mm and central wavelength of 10.5 μm. Fig. 4(b) presents the simulated focusing effect of the cross section of the focal spot at the focal plane, with FWHM of 11.6 μm and focusing efficiency value of 45.9%.

Subsequently, we fabricated the metalens via photolithography. The fabrication process involved direct utilization of pure silicon wafer to create samples with a substrate thickness of 625 μm. The process commenced with transferring the pattern from the mask plate onto the photoresist using ultraviolet lithography. This was fol-

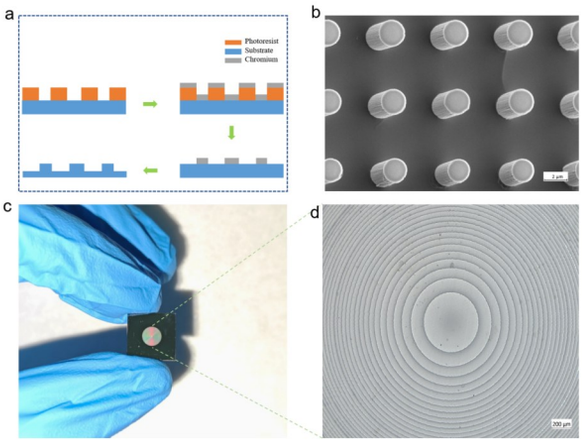

Fig. 3 The fabrication of metalens: (a) fabrication process flow diagram of the metalens; (b) local view of the fabricated metalens; (c) photograph of the fabricated metalens; (d) full view of the surface of the metalens

图3 超透镜的制作:(a)超透镜的制备工艺流程图;(b)制备的超透镜的局部图;(c)制备的超透镜的照片;(d)超透镜表面全貌

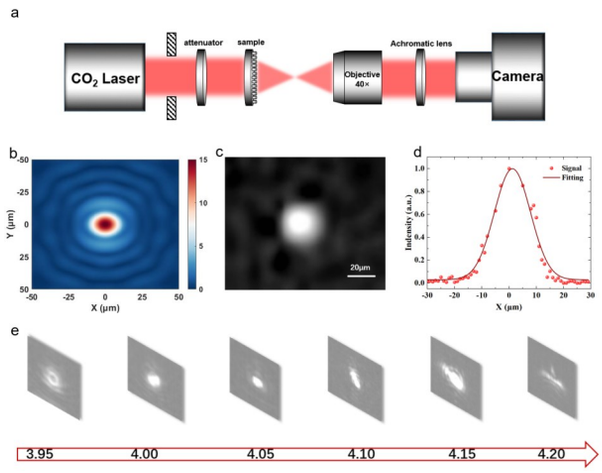

Fig. 4 Focusing performance test of the fabricated LWIR metalens: (a) index path of experiment; (b) simulation intensity of the focal plane; (c) measured power intensity across the focal plane; (d) intensity fitting of the focal spot. The original data are taken from (c); (e) image of the focal spot along the axis of the metalens

图4 制备的LWIR超透镜聚焦性能测试:(a)实验光路图;(b)模拟的焦平面电场分布;(c)实测的焦平面光强;(d)焦斑的归一化强度拟合,原始数据取自(c);(e)沿超透镜轴线拍摄的焦点图像

lowed by applying a chromium layer on the sample surface through magnetron sputtering. Afterward, we employed the lift-off process to wash off the photoresist, leaving behind the chromium pattern. Inductively coupled plasma (ICP) etching technology was used to create the metasurface and removed the remaining chromium using ceric ammonium nitrate. This process notably reduced the production budget and complexity as it employed only one-step UV lithography and ICP etching instead of low-temperature deep silicon etching. The process flow diagram is shown in Fig. 3(a). Figure 3(b-d) present photographs of the metalens sample we fabricated, along with SEM and microscopic images of its components. Figure 3(b) demonstrates the high verticality of the cylinder. The SEM images reveal that the processed patterns have an excellent morphology that meets the design requirements. The maximum aspect ratio of the structure was observed to be 3, indicating the high robustness of the nanostructures. We discovered during the experiment that increasing the etching depth appropriately can also amplify phase accumulation in the unit structure. This, in turn, broadens the focusing spot along the longitudinal direction, thereby increasing the DOF, relevant details are presented in Fig. S10 (in supplemental document).

To validate the focusing effect and practical application capability of our metalens, we designed and conducted a series of test experiments. The experimental setup, as shown in Fig. 4(a), utilized a carbon dioxide laser as the light source with a wavelength of 10.55 μm. The spot pattern before passing through the lens group is depicted in Fig. S5 (in supplemental document). The imaging equipment was composed of a 40× reflective microscope objective (Thorlabs, LMM-40X-P01), achromatic doublet infrared lenses (Thorlabs, AC254-100-E), and an uncooled thermal imaging camera (Xenics Gobi+640). This equipment was used to capture intensity images and assess the focusing performance of the metalens. A motorized stage assembly moved along the longitudinal direction (z axis) in 2.5 μm steps for the measurements. The reference position, *i. e.*, the device plane ($z = 0$), was set when the camera can clearly capture the image of the samples. Fig. S6 (in supplemental document) displays the shot of the optical path. Through the motorized stage, we measured the focal length of the metalens to be 4.05 mm, which agrees well with the designed result. Fig. 4(c) shows the cross-section of the spot at the focal plane, and Fig. 4(b) presents the focal spot image of the metalens simulated by FDTD for comparison. Tests on the focused spot, as shown in Fig. 4(d), revealed a nearly diffraction-limited FWHM of 12.6 μm. Additionally, measured Strehl ratios of the metalens is 84.1%.

Focusing efficiency is defined as the ratio of integrated power within the circle having radius $1.5 \times FWHM$ to the incident power on the metalens[49]. The focusing efficiency value for the metalens is 41.8%. When comparing the experimental performance with the simulation and theoretical performance, slight deviations from the simulation results were observed. These data were accurately computed with the aid of a Gaussian fitting function, with the focal spot after Gaussian fitting presented in Fig. S7 (in supplemental document). The deviations were attributed to discrepancies between the experimental light source and the simulated light source. In the DOF measurement, the DOF was defined as the axial distance when the maximum FWHM of the focusing spot is reduced to half. The measured DOF was approximately 11 times of the focus wavelength. Detailed results are provided in Fig. 4(e).

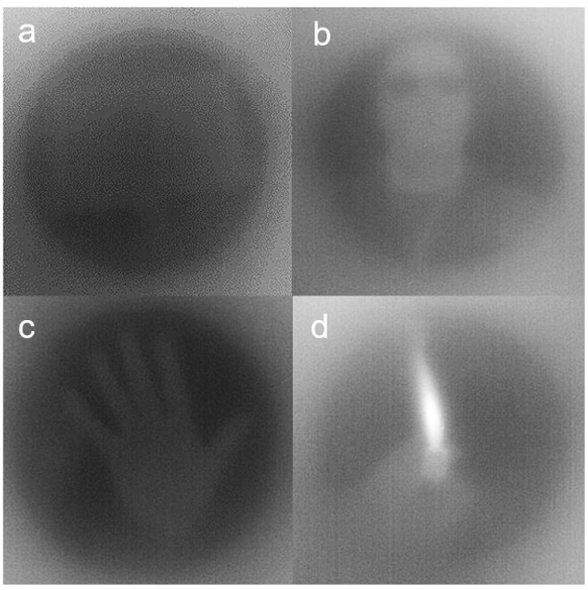

Fig. 5 Metalens imaging experiment results: (a) photograph of monitor; (b) photograph of face; (c) photograph of hands; (d) photograph of fire
图5 超透镜成像实验结果:(a)显示器;(b)人脸;(c)手;(d)火焰

Subsequently, we used the metalens for passive imaging. The experimental setup involved removing the lens of the traditional infrared camera and replacing it with our metalens. The distance between the metalens and the detector plane was adjusted, and the camera's signal was directly input into the computer for reading. The optical path diagram of the imaging experiment is given in Fig. S8(in supplemental document). We tested different targets (at the same distance) and observed good results. Fig. 5 (a-d) illustrate the infrared imaging effects of a monitor, face, palm, and candle. The camera was able to clearly capture the swinging palm and shaking individuals at 1 m distance. Owing to the large DOF, we can observe clear images even when the target was moved forward or backward over a large range of 0.4 m without refocusing. The results are presented in Fig. S9(in supplemental document).

3 Conclusions

Our successful implementation of the infrared imaging experiment demonstrates the versatility of our design. As these metalens are made of pure silicon, they are compatible with the complementary metal-oxide semiconductor (CMOS) platform and additional devices. This compatibility simplifies the building of the light path, making system miniaturization achievable.

In conclusion, this letter presents the design and fabrication of a metalens structure with a substantial DOF and broad band operation. We have demonstrated the LWIR focusing capability of an all-silicon metalens through using the thermal infrared spontaneous broadband radiation of the target to achieve passive imaging experiments. This research opens up numerous possibilities for various applications such as low-visibility imaging, robot guiding systems, and portable military detection *etc*. We are confident that the 9-11.5 μm metalens can be successfully integrated into optical systems, thereby paving the way for extensive applications in infrared imaging.

Supplemental document

Supplement materials and experimental details can be obtained by email from the authors.

References

[1] WANG S M, WU P C, SU V C, *et al*. A broadband achromatic metalens in the visible [J]. *Nature Nanotechnology*, 2018, **13**(3): 227-32.
[2] CHENG Q Q, MA M L, YU D, *et al*. Broadband achromatic metalens in terahertz regime [J]. *Sci Bull*, 2019, **64**(20): 1525-31.
[3] XIA C, LIU M, WANG J, *et al*. A polarization-insensitive infrared broadband achromatic metalens consisting of all-silicon anisotropic microstructures [J]. *Applied Physics Letters*, 2022, **121**(16): 161701.
[4] LI J, WANG Y, LIU S, *et al*. Largest aperture metalens of high numerical aperture and polarization independence for long-wavelength infrared imaging [J]. *Optics Express*, 2022, **30**(16): 28882-91.
[5] AIETA F, GENEVET P, KATS M A, *et al*. Aberration-Free Ultrathin Flat Lenses and Axicons at Telecom Wavelengths Based on Plasmonic Metasurfaces [J]. *Nano Letters*, 2012, **12**(9): 4932-6.
[6] LALANNE P, CHAVEL P. Metalenses at visible wavelengths: past, present, perspectives [J]. *Laser & Photonics Reviews*, 2017, **11**(3): 11.
[7] CHEN J, YE X, GAO S L, *et al*. Planar wide-angle-imaging camera enabled by metalens array [J]. *Optica*, 2022, **9**(4): 431-7.
[8] SARAGADAM V, HAN Z, BOOMINATHAN V, *et al*. Foveated Thermal Computational Imaging in the Wild Using All-Silicon Meta-Optics [J]. *ArXiv*, 2022, abs/2212.06345.
[9] WIRTH-SINGH A, FRöCH J E, HAN Z, *et al*. Large field-of-view thermal imaging via all-silicon meta-optics [J]. *Applied Optics*, 2023.
[10] YOON G, KIM K, HUH D, *et al*. Single-step manufacturing of hierarchical dielectric metalens in the visible [J]. *Nature Communications*, 2020, **11**(1): 10.
[11] KHORASANINEJAD M, CHEN W T, DEVLIN R C, *et al*. Metalenses at visible wavelengths: Diffraction-limited focusing and subwavelength resolution imaging [J]. *Science*, 2016, **352**(6290): 1190-4.
[12] KHORASANINEJAD M, CAPASSO F. Metalenses: Versatile multifunctional photonic components [J]. *Science*, 2017, **358**(6367): 8.
[13] CHEN X Z, HUANG L L, MUHLENBERND H, *et al*. Dual-polarity plasmonic metalens for visible light [J]. *Nature Communications*, 2012, 3.
[14] SHALTOUT A M, LAGOUDAKIS K G, VAN DE GROEP J, *et al*. Spatiotemporal light control with frequency-gradient metasurfaces [J]. *Science*, 2019, **365**(6451): 374-+.
[15] LIN R J, SU V C, WANG S M, *et al*. Achromatic metalens array for full-colour light-field imaging [J]. *Nature Nanotechnology*, 2019, **14**(3): 227-+.
[16] NDAO A, HSU L, HA J, *et al*. Octave bandwidth photonic fishnet-achromatic-metalens [J]. *Nature Communications*, 2020, **11**(1): 3205.
[17] LI L, LIU Z X, REN X F, *et al*. Metalens-array-based high-dimensional and multiphoton quantum source [J]. *Science*, 2020, **368**(6498): 1487-+.
[18] XUAN Z, LI J, LIU Q, *et al*. Artificial Structural Colors and Applications [J]. *The Innovation*, 2021, **2**(1): 100081.
[19] CHEN W T, ZHU A Y, SISLER J, *et al*. A broadband achromatic polarization-insensitive metalens consisting of anisotropic nanostructures [J]. *Nature Communications*, 2019, **10**: 7.
[20] JAVED I, KIM J, NAVEED M A, *et al*. Broad-Band Polarization-Insensitive Metasurface Holography with a Single-Phase Map [J]. *Acs Applied Materials & Interfaces*, 2022, **14**(31): 36019-26.
[21] OGAWA C, NAKAMURA S, ASO T, *et al*. Rotational varifocal moire metalens made of single-crystal silicon meta-atoms for visible wavelengths [J]. *Nanophotonics*, 2022, **11**(9): 1941-8.
[22] FENG W B, ZHANG J C, WU Q F, *et al*. RGB Achromatic Metal-

ens Doublet for Digital Imaging [J]. *Nano Letters*, 2022, **22**(10): 3969-75.
[23] BOSCH M, SHCHERBAKOV M R, WON K, *et al*. Electrically Actuated Varifocal Lens Based on Liquid-Crystal-Embedded Dielectric Metasurfaces [J]. *Nano Letters*, 2021, **21**(9): 3849-56.
[24] WEI S B, CAO G Y, LIN H, *et al*. A Varifocal Graphene Metalens for Broadband Zoom Imaging Covering the Entire Visible Region [J]. *Acs Nano*, 2021, **15**(3): 4769-76.
[25] KHORASANINEJAD M, ZHUIT A Y, ROQUES-CARMES C, *et al*. Polarization-Insensitive Metalenses at Visible Wavelengths [J]. *Nano Letters*, 2016, **16**(11): 7229-34.
[26] ARBABI A, HORIE Y, BALL A J, *et al*. Subwavelength-thick lenses with high numerical apertures and large efficiency based on high-contrast transmitarrays [J]. *Nature Communications*, 2015, **6**: 6.
[27] WANG Y L, FAN Q B, XU T. Design of high efficiency achromatic metalens with large operation bandwidth using bilayer architecture [J]. *Opto-Electronic Advances*, 2021, **4**(1): 7.
[28] WANG Y J, CHEN Q M, YANG W H, *et al*. High-efficiency broadband achromatic metalens for near-IR biological imaging window [J]. *Nature Communications*, 2021, **12**(1): 7.
[29] YOON G, KIM K, KIM S U, *et al*. Printable Nanocomposite Metalens for High-Contrast Near-Infrared Imaging [J]. *Acs Nano*, 2021, **15**(1): 698-706.
[30] SHALAGINOV M Y, AN S, ZHANG Y F, *et al*. Reconfigurable all-dielectric metalens with diffraction-limited performance [J]. *Nature Communications*, 2021, **12**(1).
[31] OU K, YU F L, LI G H, *et al*. Broadband Achromatic Metalens in Mid-Wavelength Infrared [J]. *Laser & Photonics Reviews*, 2021, **15**(9): 9.
[32] KHORASANINEJAD M, AIETA F, KANHAIYA P, *et al*. Achromatic Metasurface Lens at Telecommunication Wavelengths [J]. *Nano Letters*, 2015, **15**(8): 5358-62.
[33] FAN Z B, SHAO Z K, XIE M Y, *et al*. Silicon Nitride Metalenses for Close-to-One Numerical Aperture and Wide-Angle Visible Imaging [J]. *Physical Review Applied*, 2018, **10**(1): 10.
[34] DONG H G, WANG F Q, LIANG R S, *et al*. Visible-wavelength metalenses for diffraction-limited focusing double polarization and vortex beams [J]. *Optical Materials Express*, 2017, **7**(11): 4029-37.
[35] HUANG L, WHITEHEAD J, COLBURN S, *et al*. Design and analysis of extended depth of focus metalenses for achromatic computational imaging [J]. *Photonics Research*, 2020, **8**(10): 1613-23.
[36] BAYATI E, PESTOURIE R, COLBURN S, *et al*. Inverse designed extended depth of focus meta-optics for broadband imaging in the visible [J]. *Nanophotonics*, 2022, **11**(11): 2531-40.
[37] PAN M, FU Y, ZHENG M, *et al*. Dielectric metalens for miniaturized imaging systems: progress and challenges [J]. *Light-Science & Applications*, 2022, **11**(1).
[38] FAN Q B, LIU M Z, YANG C, *et al*. A high numerical aperture, polarization-insensitive metalens for long-wavelength infrared imaging [J]. *Applied Physics Letters*, 2018, **113**(20): 4.
[39] ZANG X F, XU W W, GU M, *et al*. Polarization-Insensitive Metalens with Extended Focal Depth and Longitudinal High-Tolerance Imaging [J]. *Advanced Optical Materials*, 2020, **8**(2): 9.
[40] HU Y Q, WANG X D, LUO X H, *et al*. All-dielectric metasurfaces for polarization manipulation: principles and emerging applications [J]. *Nanophotonics*, 2020, **9**(12): 3755-80.
[41] PETELCZYC K, BARú S, LOPEZ A C, *et al*. Imaging properties of the light sword optical element used as a contact lens in a presbyopic eye model [J]. *Optics Express*, 2011, **19**(25): 25602-16.
[42] KAKARENKO K, DUCIN I, GRABOWIECKI K, *et al*. Assessment of imaging with extended depth-of-field by means of the light sword lens in terms of visual acuity scale [J]. *Biomedical Optics Express*, 2015, **6**(5): 1738-48.
[43] ISHIZUKA N, LI J, FUJI W, *et al*. Linear polarization-separating metalens at long-wavelength infrared [J]. *Optics Express*, 2023, **31**(14): 23372-81.
[44] HUANG L, COPPENS Z, HALLMAN K, *et al*. Long wavelength infrared imaging under ambient thermal radiation via an all-silicon metalens [J]. *Optical Materials Express*, 2021, **11**(9): 2907-14.
[45] HUANG L, COPPENS Z, HALLMAN K, *et al*. All-Silicon Metalens for Long Wavelength Infrared Imaging; proceedings of the Conference on Lasers and Electro-Optics, San Jose, California, F 2022/05/15, 2022 [C]. Optica Publishing Group.
[46] YU N F, CAPASSO F. Flat optics with designer metasurfaces [J]. *Nat Mater*, 2014, **13**(2): 139-50.
[47] CHEN C, SONG W E, CHEN J W, *et al*. Spectral tomographic imaging with aplanatic metalens [J]. *Light-Science & Applications*, 2019, **8**: 8.
[48] KILDISHEV A V, BOLTASSEVA A, SHALAEV V M. Planar Photonics with Metasurfaces [J]. *Science*, 2013, **339**(6125): 1232009.
[49] BALLI F, SULTAN M A, OZDEMIR A, *et al*. An ultrabroadband 3D achromatic metalens [J]. *Nanophotonics*, 2021, **10**(4): 1259-64.